Revision 1

Word count: 8710

High-*P*-*T* phase relations of Al-bearing magnetite: Post-spinel phases as indicators for *P*-*T* conditions of formation of natural samples

LAURA UENVER-THIELE[1]
(uenver-thiele@em.uni-frankfurt.de),
ALAN B. WOODLAND[1],
NOBUYOSHI MIYAJIMA[2],
TIZIANA BOFFA BALLARAN[2],
EDITH ALIG[3],
LOTHAR FINK[3]

[1] Institut für Geowissenschaften, Goethe-Universität Frankfurt, Altenhöferallee 1, D - 60438 Frankfurt am Main, Germany

[2] Bayerisches Geoinstitut, Universität Bayreuth, D - 95440 Bayreuth, Germany

[3] Institut für Anorganische u. Analytische Chemie, Goethe-Universität Frankfurt, Max-von-Laue-Str. 7, D - 60438 Frankfurt am Main, Germany

Keywords: magnetite, hercynite, iron oxides, Fe_4O_5, Fe_7O_9, Earth's mantle, phase relations, inclusion in diamond, shock metamorphism

ABSTRACT

The phase relations of Al-bearing magnetite were investigated between 6-22 GPa and 1100-1500 °C using a multi-anvil apparatus. This study demonstrates that the spinel-structured phase persists up to ~9-10 GPa at 1100-1400 °C irrespective of the amount of hercynite ($FeAl_2O_4$) component present (20, 40 or 60 mol%). At ~10 GPa the assemblage $Fe_2(Al,Fe)_2O_5$ + $(Al,Fe)_2O_3$ forms and remains stable up to 16-20 GPa and 1200-1550 °C. $Fe_2(Al,Fe)_2O_5$ adopts the $CaFe_3O_5$-type structure with the *Cmcm* space group. At 18-22 GPa and T >1300 °C the assemblage $Fe_3(Fe,Al)_4O_9$ + $(Al,Fe)_2O_3$ becomes stable. $Fe_3(Fe,Al)_4O_9$ is isostructural with Fe_7O_9, having the monoclinic structure of the *C2/m* space group. At T <1300 °C, $Fe_3(Fe,Al)_4O_9$ + $(Al,Fe)_2O_3$ gives way to the assemblage of an hp-$Fe(Fe,Al)_2O_4$ + $(Al,Fe)_2O_3$. This hp-$Fe(Fe,Al)_2O_4$ phase is unquenchable and a defect-bearing spinel-structured phase was recovered instead; containing numerous lamellae parallel to {100} or {113} planes and notably less Al than the initial starting composition. While low-pressure spinel can have complete solid solution between Fe^{3+}-Al, the post-spinel phases have only very limited Al solubility, with a maximum of ~0.1 cpfu Al in hp-$Fe(Fe,Al)_2O_4$, ~0.3 cpfu in $Fe_2(Fe,Al)_2O_5$ and ~0.4 cpfu in $Fe_3(Fe,Al)_4O_9$, respectively. As a result, the phase relations of $Fe(Fe_{0.8}Al_{0.2})_2O_4$ can also be applied to bulk compositions richer in Al with the only difference being that larger amounts of a $(Al,Fe)_2O_3$ phase are present.

Co-existing rhombohedral-structured phases demonstrate that the binary miscibility gap established at low pressure between hematite and corundum is still valid up to 20 GPa. Since iron oxides (e.g. magnetite) with variable Al contents are found in extraterrestrial rocks or as inclusions in diamond, constraints on their high-P-T-fO_2 stability might help to unravel their formation conditions.

INTRODUCTION

Along with iron, aluminum is another notable constituent of many oxides, hydroxides, as well as silicate phases. For example, spinel group minerals are well known as important carriers for Al, along with Fe. Such minerals occur widely in the Earth's mantle and crust and are also found as accessory phases in extraterrestrial rocks (e.g. Busche et al. 1971, 1972, Keil 2012; Krot, 2019). In addition to end-member compositions spinel ($MgAl_2O_4$), hercynite ($FeAl_2O_4$), chromite ($FeCr_2O_4$), and magnetite ($Fe^{2+}Fe^{3+}{}_2O_4$), spinel-structured phases are known for their ability to form a variety of solid solutions (e.g. $MgFe_2O_4$-Fe_3O_4, Katayama and Iseda 2002; $FeAl_2O_4$-Fe_3O_4, Turnock and Eugster 1962). Of all the possible major constituents, iron, as a multi-valent element is sensitive to the prevailing redox conditions and thus can give insights into the local oxidation state within the Earth's interior. Although magnetite contains a significant amount of Fe^{3+} (Fe^{3+}/Fe_{tot}=2/3), the incorporation of other trivalent cations such as Al or Cr can lower the Fe^{3+} content and thus stabilize this phase over a larger range in oxidation states.

Previous experimental studies on the phase relations of spinel-structured oxides have demonstrated that their stability is often restricted to pressures corresponding to the upper mantle (e.g. Schollenbruch et al. 2011; Woodland et al. 2012; Uenver-Thiele et al. 2017a, 2017b; Ishii et al. 2014, 2015). At certain high-pressure (high-*P*) and high-temperature (high-*T*) conditions the spinel-structured phase can i) break down into its constituent oxides (e.g. $FeAl_2O_4$, Schollenbruch et al. 2011; $MgAl_2O_4$, Akaogi et al. 1999), ii) transform into a high-*P* polymorph (hp-O_4; e.g. Irfune et al. 1991, 2002; Funamori et al. 1998; Fei et al. 1999; Haavik et al. 2000; Levy et al. 2004; Chen et al. 2003a; Enomoto et al. 2009; Yong et al. 2012), or iii) produce an assemblage involving post-spinel phases with different stoichiometries [e.g. Fe_4O_5, Lavina et al. 2011, Woodland et al. 2012; Fe_5O_6, Lavina and Meng 2015, Woodland et al. 2015, 2023; Fe_7O_9, Sinmyo et al. 2016; $Mg_2Al_2O_5$, Enomoto et al. 2009; $Mg_2Fe_2O_5$, Boffa Ballaran et al. 2015; $(Mg,Fe)_2Fe_2O_5$ and $(Fe,Mg)_2Fe_4O_9$, Uenver-Thiele et al. 2017a, 2017b,

2018; Fe_9O_{11}, Ishii et al. 2018]. In this respect, knowing the phase relations for the chemically different post-spinel phases/assemblages can help to constrain the formation conditions and evolution of certain high-pressure samples from the Earth's mantle, from shock-metamorphosed terrestrial rocks as well as from extraterrestrial samples, forming a kind of "oxide scale" as suggested by Zhang (2017). For instance, the experimentally determined stability fields of different post-spinel assemblages in the MgO-FeO-Fe_2O_3 system over a range in *P* and *T* allowed Uenver-Thiele et al. (2017b) to add constraints on the petrological history of diamonds with inclusions of magnesioferrite ($MgFe_2O_4$). Moreover, magnesioferrite exsolutions also have been found in a number of ferropericlase (Mg,Fe)O inclusions in diamond independent of the Fe content in the ferropericlase (e.g. McCammon et al. 1998, Harte et al. 1999, Wirth et al. 2014, Kaminsky et al. 2015, Palot et al. 2016, Anzolini et al. 2019, Sharygin et al. 2021; Lorenzon et al. 2023). Such exsolution from ferropericlase may occur during ascent from the upper or lower mantle, or it may result from a back-reaction from a high-*P* precursor phase (e.g. Wirth et al. 2014, Anzolini et al. 2020). Identifying a high-*P* precursor phase often requires detailed investigation of the micro-textures of the "magnesioferrite" crystals (e.g. Jacob et al. 2016, Anzolini et al. 2020), since Fe-Mg post-spinel oxide phases can suffer from retrograde reaction during exhumation and transform or break down into a spinel-structured phase.

To the best of our knowledge, the first report of naturally preserved hp-phases was by Chen et al. (2003a, 2003b) who identified two high-*P* polymorphs of chromite with the $CaFe_2O_4$-type (CF; named "Chenmingite", IMA 2017-036, Ma and Tschauner 2017) and $CaTi_2O_4$-type (CT; named "Xieite", IMA 2007-056, Chen et al. 2008) structure preserved in the shocked Suizhou meteorite. Chen et al. (2003a, 2003b) demonstrated that these two hp-polymorphs must have formed under shock conditions of ~20-23 GPa and 1800-2000 °C. The CF-$FeCr_2O_4$ (Chenmingite) was also reported from the highly shocked Tissint Martian meteorite and is

interpreted to have formed above 16-18 GPa and temperatures below ~ 1350 °C (Ma et al. 2019). In addition, occurrences of preserved post-spinel phases have been also reported in terrestrial samples, including in a shocked gneiss from the Xiuyan impact crater (CF-type structured hp-$MgFe_2O_4$, named Maohokite, IMA 2017-047; Chen et al. 2019) or as inclusions in diamond from the Juina area, Mato Grosso State, Brazil ($CaTi_2O_4$-type structured Mg-Cr-Fe oxide and orthorhombic hp-$CaCr_2O_4$, Kaminsky et al. 2015; Maohokite, Agrosì et al. 2019). Pressure-temperature conditions of the Xiuyan impact event were estimated to be 25-45 GPa and 800-900 °C (Chen et al. 2019), while the inclusions in diamond constrained diamond formation to have occurred in the deep transition zone or lower mantle (≥18 GPa; Kaminsky et al. 2015, Agrosi et al. 2019). Note that all these *P*-*T* constraints were based upon experimental data.

Considering that high-*P* spinels occurring in both terrestrial and extraterrestrial rocks often contain significant amounts of magnetite and hercynite components (e.g. as inclusions in diamond: Newhouse & Glass 1936, Hayman et al. 2005; Stachel and Harris 2008; Kaminsky et al. 2009, Wirth et al. 2014; Palot et al. 2016, Smith et al. 2018; in extraterrestrial rocks: e.g. Keil 2012, Busche et al. 1972), knowledge about their high-*P* and high-*T* phase relations allows us to better constrain the physico-chemical conditions of their formation, as well as that of their host material. However, to date only experimental data on the phase relations of the end-member $FeAl_2O_4$ and $FeFe_2O_4$ are available and these relations are in fact quite contrasting (Schollenbruch et al. 2011, Woodland et al. 2012). Therefore, experimental investigations of solid solutions along the $FeFe_2O_4$-$FeAl_2O_4$ binary join are very important for understanding high-*P* phase stabilities in natural oxide samples containing both Fe^{3+} and Al. Here, we report the results of an experimental study on how the presence of Al affects the phase relations in $Fe(Fe,Al)_2O_4$. Since natural samples of high-*P* origin mostly have relatively low Al contents, we focussed on a Fe^{3+}-rich bulk composition (80 mol% Fe_3O_4 – 20 mol%

123 $FeAl_2O_4$), although a number of reconnaissance experiments with higher Al-contents (i.e. 40
124 mol% or 60 mol% $FeAl_2O_4$) or with a different stoichiometry of $Fe^{2+}{}_3Fe^{3+}{}_3AlO_9$ were also
125 performed.
126
127 **EXPERIMENTAL METHODS**
128
129 **Starting materials**
130 Three different starting mixtures with compositions (i) 80 mol% Fe_3O_4 – 20 mol% $FeAl_2O_4$,
131 (ii) 60 mol% Fe_3O_4 – 40 mol% $FeAl_2O_4$ and (iii) 40 mol% Fe_3O_4 – 60 mol% $FeAl_2O_4$ were
132 employed in our high-*P* experiments. A further starting composition of $Fe^{2+}{}_3Fe^{3+}{}_3AlO_9$
133 stoichiometry was employed to directly test for the extent of Al solubility in the post-spinel
134 phase Fe_7O_9. Magnetite ($FeFe_2O_4$) and hercynite ($FeAl_2O_4$) were both pre-synthesised in a
135 CO-CO_2 gas-mixing furnace at 1 atm under controlled fO_2. Magnetite was produced by
136 reducing hematite at 1300 °C and log fO_2 = -5.5, which should yield an essentially
137 stoichiometric composition (Diekmann 1982). For the synthesis of hercynite, a stoichiometric
138 mixture of Al_2O_3 and Fe_2O_3 was ground together, pressed into pellets and equilibrated at 1300
139 °C. Initially, the oxygen fugacity was set at logfO_2 = - 4 in order to first produce a mixture of
140 wüstite coexisting with a hercynite-magnetite solid solution. After 6 h, the sample was
141 quenched in water, reground and pressed into pellets for further sintering for 5 h under the
142 same conditions. This procedure was repeated for additional two cycles, but with a stepwise
143 shift to more reducing conditions (logfO_2 = - 9 for 4 h; logfO_2 = - 11.4 for 1 h) to ensure all of
144 the iron is Fe^{2+} in the final step. A direct synthesis at low fO_2 tends to produce a mixture of
145 metallic Fe and corundum, which then does not react efficiently to hercynite. Several crystals
146 of magnetite and hercynite were checked for homogeneity and chemical composition by
147 electron microprobe (EPMA). Analysis of X-ray powder diffraction patterns gave a unit-cell
148 parameter for magnetite and hercynite of a_0= 8.3966(6) Å or a_0= 8.1502(1) Å, respectively.

149 The starting material of $Fe^{2+}_3Fe^{3+}_3AlO_9$ was composed of a stoichiometric mixture of
150 $FeAl_2O_4$, $FeFe_2O_4$, Fe_2O_3 and Fe^0 in a 1:2:2:1 molar ratio. To prevent adsorption of moisture,
151 the starting materials were stored in a desiccator.
152
153 **Experimental procedure**
154 High-*P* and high-*T* experiments were performed at the Goethe Universität Frankfurt and the
155 Bayerisches Geoinstitut in Bayreuth over a *P*-*T* range of 6-22 GPa and 1200-1600 °C (see
156 Table 1). Experimental run conditions and run products are listed in Table 1. Experiments up
157 to 14 GPa and some at 18 GPa were performed in Frankfurt using an 800t Walker-type multi-
158 anvil apparatus (Walker et al. 1990). Experiments carried out at the Bayerisches Geoinstitut
159 Bayreuth were conducted with 500t, 1000t or 5000t split-sphere Kawai-type multi-anvil
160 presses (Kawai and Endo 1970). Mineral phase transitions (e.g. α-Mg_2SiO_4–β-Mg_2SiO_4, β-
161 Mg_2SiO_4–γ-Mg_2SiO_4, coesite-stishovite, $CaGeO_3$ garnet–perovskite, $MgSiO_3$ ilmenite-
162 perovskite) were used for pressure calibration with details described in Brey et al. (2008) and
163 Keppler and Frost (2005). Different assembly sizes were used depending on the desired
164 pressure. Up to 14 GPa, Cr_2O_3-doped MgO octahedra were employed along with tungsten
165 carbide (WC) cubes having 8 mm truncation edges (so-called 14/8 assembly). Higher-
166 pressure experiments were conducted using 10/4, 10/5, 18/8 or 18/11 assemblies/truncation
167 lengths. The pressure cells in Frankfurt have a Re-foil heater, whereas $LaCrO_3$ was employed
168 as a heater in the experiments at the Bayerisches Geoinstitut. The heater was placed inside
169 either in a ZrO_2 or a $LaCrO_3$ (only for 10/4 experiments with Re-foil heater) sleeve, which
170 acts as a thermal insulator. While the Re-foil had direct contact with the WC cubes, a
171 molybdenum ring and disc was inserted at the top or the bottom of the $LaCrO_3$ heater to
172 ensure contact to the WC cubes. The sample capsule/s and thermocouple were surrounded by
173 MgO sleeves to avoid direct contact with the furnace. The starting material was usually
174 loaded into Ag-foil capsules, however, several experiments employed Pt-foil when the desired

temperature exceeded the melting point of Ag. Capsule dimensions depended on the particular assembly employed with 1.2 to 2 mm diameter and 1.2 to 1.7 mm length. Either a W_5/Re_{95}–W_{26}/Re_{74} thermocouple (800t multi-anvil press) or a W_3/Re_{97}–W_{25}/Re_{75} thermocouple (1000t, 5000t multi-anvil press) was inserted axially from the top of the octahedron to monitor the temperature, with the electromotive force uncorrected for pressure. Further details of the experimental setup are described in Brey et al. (2008) and Keppler and Frost (2005). Uncertainties in pressure and temperature are ±0.5 GPa and ±30-50 °C, respectively (Keppler and Frost 2005). The experiments were conducted first by cold pressurization, followed by heating to the desired temperature at a rate of 50 °C/min. The experiment was terminated by turning off the power while maintaining the pressure. Depending on the experimental *P-T* conditions, the duration varied from 1 to 3 hrs (see Table 1). After quenching, decompression was immediately initiated.

Analytical methods

The recovered samples were analysed with electron microprobe (EPMA), powder X-ray diffraction and/or transmission electron microscope (TEM). For chemical analyses, several fragments of the recovered sample were mounted in epoxy, polished and carbon-coated. Measurements were carried out with a five-spectrometer JEOL JXA-8530F plus Hyperprobe at the University of Frankfurt operating in the wavelength-dispersive mode with an acceleration voltage of 15 kV, probe current of 20 nA and a spot size of 1 µm. Pure Fe_2O_3, Al_2O_3 and Pt metal were employed as primary standards. Integration times for Al were 20 s on the peak and 10 s on the background while 40 s on the peak and 20 s on the background were adjusted for Fe and Pt. A CITZAF algorithm was employed for the matrix correction (Armstrong 1993). For investigating microtextures and verifying the homogeneity of the mineral grains, backscatter electron images were taken (e.g. Fig. 1a-d).

Further phase identification by X-ray diffraction was performed using an STOE Stadi P diffractometer equipped with a linear PSD or a Mythen detector and a Ge(111) monochomator at the University of Frankfurt operating at 45 kV and 35 mA and using MoKα (λ=0.70926 Å) radiation. Recovered sample material and small amounts of silicon which served as internal standard were ground together and mounted in a 0.5 mm diameter glass capillary. Measurements were performed in Debye-Scherrer mode in transmission geometry between 1-100° 2θ. Determination of the unit-cell parameters was obtained by full-pattern refinement using the general structure analysis system (GSAS; Larson and von Dreele 1994) software package and the EXPGUI interface of Toby (2001).

Two samples (S7316; Z1953o) had (i) not enough sample material for powder X-ray diffraction and/or (ii) included phases with breakdown textures so that TEM analyses were necessary. Those run products were investigated using a FEI Titan G2 80-200 S/TEM equipped with 4 SDD energy-dispersive X-ray spectrometers (EDS) and a Philips CM20FEG with a pure Ge EDS, operating at 200 kV at the Bayerisches Geoinstitut Bayreuth (Germany). Some of the recovered sample material was cut and polished to make a thin section. The thin section was placed on a 3-mm-sized Mo grid and thinned to electron transparency by Ar-ion milling at accelerating voltages of 3.5 kV and an angle of incident of 8° using a precision ion polishing system (Gatan, model 691). The sample foil was carbon-coated to reduce charging and then investigated by imaging microtextures, selected area electron diffraction (SAED) and energy-dispersive X-ray (EDX) analyses. In addition, a part of the recovered material of sample Z1953o was polished on the surface and thinned to electron transparency by using a focused Ga ion beam (FIB) milling machine (FEI, Scios Dual Beam system) at the Bayerisches Geoinstitut Bayreuth (Germany).

RESULTS AND DISCUSSION

225

226 **Experimental run products**

227 The resulting phase assemblages, as well as chemical compositions and lattice parameters of
228 the individual phases, are summarized in Tables 1, 2 and 3. A total of 20 experiments with the
229 $Fe^{2+}(Fe^{3+}_{0.8}Al_{0.2})_2O_4$ starting composition were performed over a *P*-*T* range of 6-22 GPa and
230 1100-1550 °C. A limited number of experiments were performed with higher Al contents
231 corresponding to stoichiometries of $Fe^{2+}(Fe^{3+}_{0.6}Al_{0.4})_2O_4$ and $Fe^{2+}(Fe^{3+}_{0.4}Al_{0.6})_2O_4$ (Table 1).
232 These experiments were performed to clarify the extent of Al solubility in the high-*P* post-
233 spinel phases. Following the identification of a phase with $(Fe^{2+})_3(Fe^{3+},Al)_4O_9$ stoichiometry
234 (O_9-phase; see text below), two further experiments with a starting composition of
235 $Fe^{2+}_2Fe^{3+}_2AlO_9$ were specifically performed to investigate the maximum amount of Al that
236 can be incorporated into this phase.

237 Backscattered electron (BSE) imaging of the run products confirms noticeable grain growth
238 (2-60 μm in size) with complete recrystallization into chemically homogenous grains. Straight
239 grain boundaries and triple junctions often with grain boundary angles of ~120° in the
240 polycrystalline samples indicate that an "equilibrium-fabric" was reached during the
241 experiments (Fig. 1a-d; Passchier and Trouw, 2005). The apparent even distribution of the
242 newly formed phases (Fig. 1), indicates that the starting material was well homogenized. One
243 exception is sample Z1953o, which includes an additional phase that exhibits internal textures
244 of very fine-grained crystals (Fig. 1d) indicating that this phase dissociated during quench
245 (unquenchable phase; named hereafter UQ-phase). The Fe^{2+}-bearing oxide phases always
246 form the largest grains while interstitial corundum-hematite solid solutions are much smaller
247 in size.

248

249 **Phase relations of $Fe^{2+}(Fe^{3+}_{0.8}Al_{0.2})_2O_4$**

Breakdown into $Fe_2(Fe,Al)_2O_5$ + $(Al,Fe)_2O_3$

Low-pressure experiments demonstrate that the stability of the spinel-structured phase persists up to about 9-10 GPa at temperatures of 1200-1400 °C (Fig. 2). In most cases, this phase has a composition similar to that of the initial starting mixture (see Table 2). At higher pressure, the spinel-structured phase breaks down to a multi-phase assemblage as indicated by BSE imaging and X-ray powder diffraction. Analysis of diffraction patterns (Online Materials Fig. OM1) reveals an $A_2B_2O_5$ phase with a $CaFe_3O_5$-type structure (space group *Cmcm*, Lavina et al. 2011; Boffa Ballaran et al. 2015) coexisting with one or two corundum-type structured phases (space group *R-3c*) having $(Fe,Al)_2O_3$ stoichiometry. The O_5-structured phase is equivalent to those found in the Fe^{2+}-Fe^{3+} and Mg-Fe^{3+} endmember systems (e.g. Woodland et al. 2012; Uenver-Thiele et al. 2017a, 2017b). Siderite appeared in some experiments in trace amounts, barely detectable in most powder diffraction patterns. We attribute its presence to the reaction of adsorbed CO_2 with the fine-grained starting material powders, which implies minor reduction of Fe^{3+} to Fe^{2+} during the experiment. In experiment M815, tiny amounts of a Fe_5O_6 structured phase (Lavina and Meng 2015; Woodland et al. 2015, 2023) were identified in the powder XRD pattern. Its presence might be also attributed to a small degree of reduction during the experiment.

In terms of composition, the O_5-phase contains relatively low amounts of Al, with only up to 0.3 cpfu present, corresponding to 15 mol% $Fe_2Al_2O_5$ component (Table 2). Thus, this phase incorporated proportionally less Al than present in the starting material (i.e. $(Al/(Al+Fe^{3+})$ = 0.15 compared to 0.2 in the starting composition). The Al poorer and Fe^{2+} richer stoichiometry of the O_5-phase compared to the starting bulk composition causes an excess of trivalent cations (Al and Fe^{3+}) that stabilises the coexisting corundum-hematite solid solutions (herafter referred to as cor_{ss} or hem_{ss} depending on the Al/Fe ratio, Table 1). In many experiments two separate phases were present, indicating that the large miscibility gap along

This is the peer-reviewed, final accepted version for American Mineralogist, published by the Mineralogical Society of America.
The published version is subject to change. Cite as Authors (Year) Title. American Mineralogist, in press.
DOI: https://doi.org/10.2138/am-2023-8948. http://www.minsocam.org/

the Al_2O_3-Fe_2O_3 binary documented by Feenstra et al. (2005) at <4.0 GPa and 1300 °C persists to at least 18 GPa (Table 1). For instance, this is manifested in the coexistence of hematite with up to 23.5 mol% Al_2O_3 (hem_{ss}) and corundum with up to 10.5 mol% Fe_2O_3 (cor_{ss}) in many of our experiments (see Table 1 and Table 3).

Stability of $Fe^{2+}_3(Fe^{3+},Al)_4O_9$ + $(Al,Fe)_2O_3$

In the *P*-*T* range of 16-20 GPa and 1200-1550 °C, the maximum stability of the O_5-phase is reached and above such pressures another phase assemblage becomes stable (Figs. 1 and 2). The XRD patterns of run products from four experiments (Z2040u, M841, H5668, H5745) indicate the presence of a Fe_7O_9-structured phase (Sinmyo et al. 2016) (see Fig. 1b, Online Materials Fig. OM2, and Table 1). In experiment Z2040u and H5668, $Fe_3(Al,Fe)_4O_9$ represents the majority phase together with hem_{ss} and/or cor_{ss} (Fig. 1b). The sample is well crystallized with no apparent reaction zones (Fig. 1b). Coexisting cor_{ss}, also occurring as inclusions in the O_9-phase indicate that the O_9-phase was saturated in Al. Thus, under the conditions of our experiments, it appears that only up to 10.5 mol % of a $Fe_3Al_4O_9$ component can be incorporated into Fe_7O_9.

The appearance of $Fe_3(Fe,Al)_4O_9$ is notable since no O_9-phase has been observed in the phase relations of either the Fe_3O_4 or $FeAl_2O_4$ endmembers (e.g. Woodland et al. 2012, Schollenbruch et al. 2011). However, it is likely that further new studies of different spinel compositions will also reveal the stability of an O_9-phase. For example, Uenver-Thiele et al. (2017b) reported the existence of $Mg_3Fe_4O_9$ and $Mg_{1.5}Fe_{1.5}Fe_4O_9$ in the $MgFe_2O_4$ and $Mg_{0.5}Fe^{2+}_{0.5}Fe_2O_4$ systems, respectively. More recently, Ishii et al. (2020) also studied the high-*T* and high-*P* phase relations of $MgFe_2O_4$. Their study confirmed the existence of an O_9-phase + hem assemblage, but at a somewhat different *P*-*T* range (Ishii et al. 2020) than reported earlier. In any case, both studies of Mg-bearing compositions indicate that an O_9-structured phase becomes stable at pressures beyond the stability of an M_4O_5 + hem

This is the peer-reviewed, final accepted version for American Mineralogist, published by the Mineralogical Society of America.
The published version is subject to change. Cite as Authors (Year) Title. American Mineralogist, in press.
DOI: https://doi.org/10.2138/am-2023-8948. http://www.minsocam.org/

assemblage and its stability appears to be limited to a narrow range in *P*-*T* space. Here, in Al-bearing compositions, we also find that the stability of $Fe_3(Fe,Al)_4O_9$ is limited to a narrow range in *P* and *T* beginning at ~18 GPa (at 1300-1400 °C) and widens to higher *P* and *T* (at 20 GPa >1300 °C but <1550 °C; see Fig. 2).

Appearance of a hp-polymorph

As previously described, $Fe_3(Fe,Al)_4O_9$ becomes stable at $P \geq 18$ GPa and $T \geq 1300$ °C. At 18 GPa and 1300 °C (M841) run products include an O_9-phase together with cor_{ss} as well as an additional phase. At lower *T* the O_9-phase completely disappears. Analysis of the XRD patterns suggests that a spinel-structured phase with a lattice parameter of a =8.3696(4) - 8.3830(1) Å is present. However, low-pressure experiments indicate that the spinel-structured $Fe^{2+}(Fe^{3+}_{0.8}Al_{0.2})_2O_4$ phase has its maximum pressure stability at 9-11 GPa with a lattice parameter of a =8.3379(1) Å (e.g. sample M840; Table 1, Fig. 2). Chemical analyses by EPMA and TEM (see Table 2) reveal that this phase (at ≥18 GPa) has an extremely low Al content, approaching an almost pure magnetite composition [$Fe^{2+}(Fe^{3+}_{0.95}Al_{0.05})_2O_4$], which is consistent with the observed lattice parameter. However, since experimental studies have demonstrated that magnetite is also only stable up to 9-10 GPa (e.g. Woodland et al. 2012, Fig. 2) this phase in experiments at ≥18 GPa must be a product of a retrograde back-reaction from a high-*P* phase during quenching. To clarify the presence or even the nature of the precursor phase of the magnetite, sample S7316 and Z1953o were investigated by TEM, with sample Z1953o being discussed in more detail since it contains not only a spinel-structured phase but also an UQ-phase (see Figs. 1d and 3a). Striations within this magnetite-rich spinel observed by BSE imaging were investigated in detail and proved to be numerous lamellae (Fig. 3). Some of these lamellae have an orientation corresponding to the {113} plane in the magnetite (Fig. 3c), which is consistent with the orientation of {113} twins. The twinning

along {113} usually reflects a back reaction from a galena-like archetype structure belonging to the lillianite homologies series (Makovicky 1977) and as such may result from the back-reaction of a hp-phase like Fe_4O_5 or Fe_5O_6 (Schollenbruch et al. 2011; Woodland et al. 2012, 2023; Myhill et al. 2016). Since the lamellae within the magnetite of sample Z1953o are not only on the {113} plane but also on the {100} plane and $Fe_3(Fe,Al)_4O_9$ is quenchable without any retrograde microtextures, we interpreted this defect magnetite (dmt) phase to be indicative of a previous high-*P* orthorhombic O_4-polymorph (e.g., Haavik et al. 2000). However, although the {100} and {113} lamellae seem to have twin-like features, their twin law remains to be determined and statistically proven, and the stability of this hp-polymorph at *P* and *T* needs to be verified by in-situ high-*P*-*T* experiments.

Detailed TEM observations of the UQ-phase confirm that it results from the dissociation into two phases (Fig. 4) during quench. The new nanometer-sized crystals are vermicularly intergrown, a texture that is commonly known for exsolution processes within minerals (e.g. feldspar). Moreover, TEM observations indicate that the crystals are in an epitaxial relation with the larger surrounding crystals, which is not expected if they crystallized from a melt. As can be seen from EDS chemical map illustrated in Figure 4b the dissociation products are either Al- or Fe-rich. The electron diffraction patterns of the Al-dominant phase are consistent with a corundum structure (Fig. 4c), while those of the Fe-dominant phase correspond to a spinel structure (i.e., magnetite) (Fig. 4d). It is noteworthy that this magnetite within the UQ-domain differs from the dmt described above. For instance, the magnetite within the UQ-phase does not have the characteristic relict features expected for transformation from a previous hp-polymorph. This phase is also richer in Al-content than the dmt phase.

Crystal-chemical behaviour of high-*P* phases

Influence of Al on the stability of hp-phases

A few experiments were performed with magnetite solid solutions having higher Al contents. Experiments with starting compositions of $Fe(Fe_{0.6}Al_{0.4})_2O_4$ or $Fe(Fe_{0.4}Al_{0.6})_2O_4$ produced post-spinel assemblages similar to those obtained with lower bulk Al contents, such as $Fe_2(Fe,Al)_2O_5$ + $(Fe,Al)_2O_3$ or $Fe_3(Fe,Al)_4O_9$ + $(Fe,Al)_2O_3$ (Table 1). The appearance of these assemblages occurred at about the same *P-T* range as for the $Fe(Fe_{0.8}Al_{0.2})_2O_4$ bulk composition. This is due to the limited incorporation of Al in the O_5 and O_9 phases so that their compositions do not differ significantly from those synthesized with a $Fe(Fe_{0.8}Al_{0.2})_2O_4$ bulk composition. Thus, phase relations of $Fe(Fe_{0.8}Al_{0.2})_2O_4$ (shown in Fig. 2) are also valid at higher bulk Al contents, the only difference being a higher proportion of cor_{ss} and hem_{ss} in the assemblage.

Fe_4O_5-$Fe_2Al_2O_5$ solid solutions

The molar volume of the Fe_4O_5 phase decreases strongly and linearly with increasing Al content (Fig. 5a). This behaviour can be explained by the substitution of the smaller Al^{3+} cation for Fe^{3+} (ionic radius = 53.5 vs. 64.5 pm, respectively, Shannon 1976). The decrease in molar volume is mostly due to changes in the *b*- and *c*-parameters (Fig. 5c-d). The *a*-lattice parameter does not significantly change with composition (Fig. 5b). This implies that little to no Al substitution occurs on the prismatic M3 site and is consistent with the observation of Boffa Ballaran et al. (2015) that this site is dominated by divalent cations. As already indicated, Al^{3+} substitution for Fe^{3+} in the O_5-phase is quite limited. The reason for this may be that the observed large changes in unit-cell parameters with Al incorporation act to destabilise the crystal structure. This contrasts with the successful synthesis of a $Fe_2Cr_2O_5$ endmember (Ishii et al. 2014), probably because Cr^{3+} has an ionic radius much more similar to that of Fe^{3+} (61.5 pm, Shannon 1976).

Al-substitution in Fe_7O_9

The crystal structure of Fe_7O_9 is monoclinic and comprises four different crystallographic sites for cations (Fe1, Fe2, Fe3, Fe4); Fe1, Fe2 and Fe3 are edge-sharing octahedra and the Fe4 site is trigonal prismatic (Sinmyo et al. 2016). Sinmyo et al. (2016) indicate that the Fe4 site is almost fully occupied by Fe^{2+}. Therefore, we consider that in our $Fe_3(Al,Fe)_4O_9$ phase, Al will substitute for Fe^{3+} at the Fe1, Fe2 and Fe3 octahedral sites whereas the Fe4 site will be occupied by Fe^{2+}. This distribution is consistent with our limited lattice parameter data for Al-bearing Fe_7O_9. The *b*-parameter, which is mostly controlled by the height of the trigonal prism, does not vary significantly with Al content. On the other hand, we find that even small amounts of Al (e.g. 0.22-0.33 cpfu; see Table 2) substitution lead to a significant shortening in the *a*- and c-parameters. The *a*-parameter is the direction of the edge-sharing octahedral strips containing the Fe1, Fe2 and Fe3 sites in the structure and the stacking direction of these strips is along the *c*-axis (Sinmyo et al. 2016). Based upon the coexistence with a corundum solid solution in our experiments, it appears that the maximum Al content that the O_9-phase can accommodate is even more limited than observed for the O_5-phase.

Fe_2O_3-Al_2O_3 solid solutions

In most experiments, Fe^{3+}-bearing corundum coexists with other high-*P* Fe-Al-oxides (Table 1). In five experiments, both Fe-bearing corundum and Al-bearing hematite are present (Table 1). The chemical compositions and lattice parameters for these two phases are given in Table 3. It is notable that the chemical compositions of coexisting hem_{ss} and cor_{ss} from our experiments are faithfully consistent with the binary miscibility gap observed at much lower pressures of ≤ 4 GPa (Fig. 6, Feenstra et al. 2005; Turnock & Eugster 1962; Atlas & Sumida 1958). In addition, our unit-cell–composition systematics agree very well with those reported by Feenstra et al. (2005) (Fig. 7). This implies that the mixing behaviour along the hematite–corundum binary described by Feenstra et al. (2005) is still valid for pressures up to 20 GPa.

In some experiments, the cor_{ss} does not coexist with a hem_{ss} and is therefore not necessarily Fe^{3+}-saturated.

IMPLICATIONS

Recent experimental syntheses of new high-pressure post-spinel phases with stoichiometries of M_4O_5, M_5O_6, M_7O_9, and M_9O_{11} give rise to the question if these phases might occur in natural samples. Since they are all stable over certain ranges in *P* and *T*, they could serve as "index phases" indicative of the conditions the host sample experienced (e.g. deep mantle or shock-metamorphosed samples). For instance, diamonds and their inclusions provide a unique opportunity to directly study pristine material from great depths in the Earth's mantle. Several studies report exotic non-ultramafic (non-silicate) inclusions from uncertain or controversial depths (e.g. Hayman et al. 2005). In some cases, magnetite has been identified either as discrete grains or associated with other phases such as wüstite, metallic alloy, hematite or pyrrhotite (e.g. Anzolini et al. 2019, 2020, Shirey et al. 2019, Jacob et al. 2011, 2016, Wirth et al. 2014, Hayman et al. 2005, Stachel et al. 1998, Hutchison 1997). Since end-member magnetite is stable only up to ~10 GPa, the logical interpretation is that such inclusions formed in the upper mantle. However, the occurrence of particular microstructures in magnetite can be an indicator that it formed as a breakdown product from a precursor phase (e.g. Jacob et al. 2016, Anzolini et al. 2020). For example, Jacob et al. (2016) reported framesitic diamond with inclusions of pyrrhotite that had a partially developed nanocrystalline reaction rim of magnetite. Based on the epitaxial growth of pyrrhotite, magnetite and diamond, Jacob et al. (2016) concluded that magnetite formed at the expense of pyrrhotite directly, followed by the precipitation of diamond on this magnetite corona. In performing Transmission Kikuchi Diffraction (TKD) analyses, they identified twinning on the {311} planes (note, the {311} plane is equivalent to the {113} plane (Fig.3c) in the cubic

system), a textural feature shown to occur as a consequence of a breakdown of $Fe_4O_5 + Fe_2O_3$ or $Fe_4O_5 + O_2$ (Woodland et al. 2012, Myhill et al. 2016). Thus, Uenver-Thiele et al. (2017b) interpreted this twinning in the natural magnetite to be the first evidence for the natural occurrence of an O_5-phase in a mantle sample. Since magnetite both with and without {311} twinning was present in the diamond, Uenver-Thiele et al. (2017b) considered the origin of these inclusions to lie in the upper mantle between 8-10 GPa, conditions at which Fe_4O_5 and magnetite can coexist (Myhill et al. 2016; Schollenbruch et al. 2011; Woodland et al. 2012). Nevertheless, twinning on the {311} planes in magnetite can also result from the retrograde reaction of other iron oxide phases such as Fe_5O_6 (Woodland et al. 2023). On the other hand, the {100} and {113} lamellae in our recovered defect magnetite, which we interpret to have formed from a hp-O_4 phase at *P* and *T* (see above), can also help to distinguish one precursor candidate from another. This means that detailed documentation of twinning features and lamellae textures are important in future studies of experimental and natural samples.

The results of this present work also demonstrate that the composition of phases in the Fe^{2+}-Fe^{3+}-Al-oxide system can help to discriminate whether a spinel-structured phase formed from a precursor phase or not. In contrast to spinel-structured phases, the high-*P* post-spinel phases in this study are found to incorporate only minor amounts of Al (~0.1 cpfu Al in a hp-O_4 polymorph, ~0.3 cpfu Al in $A_2B_2O_5$ or ~0.4 cpfu in $A_4B_3O_9$). This implies that any spinel that formed from a higher-*P* precursor phase must also have a low Al content. In fact, spinels occurring as inclusions in diamond generally have low Al contents (Hayman et al. 2005; Wirth et al. 2014; Palot et al. 2016; Anzolini et al. 2020), but this may also be due to formation in a low-Al environment. For such compositions, our current results indicate that the phase relations of $Mg_{0.5}Fe_{0.5}Fe_2O_4$ presented by Uenver-Thiele et al. (2017b) are still applicable. On the other hand, Wirth et al. (2014) reported Al-rich spinels with compositions ~$(Mg_{0.73}Fe_{0.25}Mn_{0.02})(Fe_{0.44}Al_{1.17}Cr_{0.39})O_4$ occurring together with magnetite-magnesioferrite

solid solutions within a magnesiowüstite (MW) inclusion in a diamond from Brazil. Since the Al-rich spinels were found to be in epitaxial relationships with the host MW and the nearly Al-free magnesioferrite/magnetite, Wirth et al. (2014) considered that their exsolution from the MW host must have taken place under the same *P-T* conditions predicted for the magnesioferrite/magnetite. Our current study indicates that this Al-rich spinel could not have initially formed as a post-spinel phase. However, the high Mg content reported by Wirth et al. (2014) may also suggest that in this case the spinel structure was stabilized to higher pressures, up to ~15-16 GPa at ~1200-1600 °C (Akaogi et al. 1999). The effect of Mg on phase relations is the subject of an ongoing study (Uenver-Thiele et al. in prep). In any case, in Al-rich bulk compositions at *P-T* conditions above spinel stability, an additional Al-rich phase like corundum or garnet would be expected to coexist with low-Al oxide phases, like those described here.

Acknowledgements

This study was supported by the Deutsche Forschungsgemeinschaft (DFG) to A.B.W. (Wo 652/20-2) and T.B.B. (Bo 2550/7-2). We are grateful to Thomas Kautz, Nicki Siersch, Svyatoslav Shcheka, Caterina Melai and Tony Withers for their technical advice and assistance with the multi-anvil experiments at the University of Frankfurt and the Bayerisches Geoinstitut Bayreuth. Thanks to Nils Pravitz, Raphael Niul and Dorothea Wiesner for sample preparation and preparation of a FIB lamella, respectively. Lea Ruckes is thanked for technical support with the electron microprobe. We acknowledge the DFG for funding the FIB facility (grant INST 91/315-1 FUGG) and the TEM facility (grant INST 91/251-1 FUGG). We would also like to acknowledge two anonymous reviewers for their valuable feedback, which helped to significantly improve this manuscript.

REFERENCES

Agrosì, G., Tempesta, G., Mele, D., Caggiani, M.C., Mangone, A., Della Ventura, G., Cestelli-Guidi, M., Allegretta, I., Hutchison, M.T., Nimis, P., and Nestola, F. (2019) Multiphase inclusions associated with residual carbonate in a transition zone diamond from Juina (Brazil). Lithos, 350-351, 105279.

Akaogi, M., Hamada, Y., Suzuki, T., Kobayashi, M., and Okada, M. (1999) High pressure transitions in the system $MgAl_2O_4$–$CaAl_2O_4$: a new hexagonal aluminous phase with implication for the lower mantle. Physics of the Earth and Planetary Interiors, 115, 67–77.

Anzolini, C., Nestola, F., Mazzucchelli, M., Alvaro, M., Nimis, P., Gianese, A., Morganti, S., Marone, F., Campione, M., Hutchison, M., and Harris, J. (2019) Depth of diamond formation obtained from single periclase inclusions. Geology, 47, 219-222, doi: 10.1130/G45605.1

Anzolini, C., Marquardt, K., Stagno, V., Bindi, L., Frost, D.J., D. Pearson, G., Harris, J.W., Hemley, R.J., and Nestola, F. (2020) Evidence for complex iron oxides in the deep mantle from FeNi(Cu) inclusions in superdeep diamond. Proceedings of the National Academy of Sciences, 117, 35, doi: 10.1073/pnas.2004269117

Atlas, L.M., and Sumida, W.K. (1958) Solidus, subsolidus, and subdissociation phase equilibria in the system Fe-Al-O. Journal of the American Ceramic Society, 41, 150-160.

Armstrong, J.T. (1993) Matrix correction program CITZAF, Version: 3.5, California Institute of Technology

503 Boffa Ballaran, T., Uenver-Thiele, L., Woodland, A.B., and Frost, D.J. (2015) Complete
504 substitution of Fe^{2+} by Mg in Fe_4O_5: The crystal structure of the $Mg_2Fe_2O_5$ end-member.
505 American Mineralogist, 100, 628-632.
506
507 Brey, G.P., Bulatov, V., and Girnis, A. (2008): Geobarometry for peridotites: experiments in
508 simple and natural systems from 6 to 10 GPa. Journal of Petrology, 49, 3–24.
509
510 Busche, F.D., Conrad, G.H., Keil, K., Prinz, M., Bunch, T.E., Erlichman, J.E., and Quaide,
511 W. L. (1971) Electron microprobe analyses of minerals from Apollo 12 lunar samples.
512 Department of Geology & Institute of Meteoritics, University of Mexico, Special Publication,
513 3, 61.
514
515 Busche, F.D., Prinz, M., and Keil, K. (1972) Spinels and the petrogenesis of some Apollo 12
516 igneous rocks. American Mineralogist, Vol. 57, 1729-1747.
517
518 Chen, M., Shu, J., Mao, H-k., Xie, X., and Hemley, R.J. (2003a) Natural occurrence and
519 synthesis of two new post spinel polymorphs of chromite. Proceeding of the national academy
520 of sciences, 100, 14651-14654.
521
522 Chen, M., Shu, J., Xie, X., and Mao, H.-K. (2003b) Natural $CaTi_2O_4$-structured $FeCr_2O_4$
523 polymorph in the Suizhou meteorite and its significance in mantle mineralogy. Geochimica et
524 Cosmochimica Acta, 67, 3937-3942.
525
526 Chen, M., Shu, J., and Mao, H. (2008) Xieite, a new mineral of high-pressure $FeCr_2O_4$
527 polymorph. Chinese Science Bulletin 53, no.21, 3341-3345.
528

529 Chen, M., Shu, J., Xie, X., and Tan, D. (2019) Maohokite, a post-spinel polymorph of
530 $MgFe_2O_4$ in shocked gneiss from the Xiuyan crater in China. Meteoritics and Planetary
531 Science, 54, 495-502.
532
533 Dieckmann, R. (1982). Defects and Cation Diffusion in Magnetite (IV): Nonstoichiometry
534 and Point Defect Structure of Magnetite ($Fe_{3-\delta}O_4$). Bericht der Bunsenges. Journal of Physical
535 Chemistry, 86, 112-118.
536
537 Enomoto, A., Kojitani, H., Akaogi, M., Miura, H., and Yusa, H. (2009) High-pressure
538 transitions in $MgAl_2O_4$ and a new high-pressure phase of $Mg_2Al_2O_5$. Journal of Solid State
539 Chemistry, 182, 389-395.
540
541 Fei, Y., Frost, D.J., Mao, H.-K., Prewitt, C.T., and Häusermann, D. (1999) In situ
542 determination of the high-pressure phase of Fe_3O_4. American Mineralogist, 84, 203-206.
543
544 Finger, L.W., and Hazen, R.M. (1980) Crystal structure and isothermal compression of Fe_2O_3,
545 Cr_2O_3 and V_2O_3 to 50 kbars. Journal of Applied Physics, 51, 5362-5367.
546
547 Feenstra, A., Sämann, S., and Wunder, B. (2005) An Experimental Study of Fe-Al Solubility
548 in the System Corundum-Hematite up to 40 kbar and 1300 °C. Journal of Petrology, 46, 1881-
549 1892. doi: 10.1093/petrology/egi038.
550
551 Funamori, N., Jeanloz, R., Nguyen, J. H., Kavner, A., Caldwell, W. A., Fujino, K., et al.
552 (1998). High-pressure transformations in $MgAl_2O_4$. Journal of Geophysical Research,
553 103(B9), 20, 813–20,818. doi: 10.1029/98JB01575

Haavik, C., Stølen, S., Fjellvåg, H., Hanfland, M., and Häusermann, D. (2000) Equation of state of magnetite and its high-pressure modification: Thermodynamics of the FeO system at high pressure. American Mineralogist, 85, 514-523.

Harte, B., Harris, J.W., Hutchison, M.T., Watt, G.R., and Wilding, M.C. (1999) Lower mantle mineral associations in diamonds from Sao Luiz, Brazil. In F.R. Boyd, Y. Fei, C.M. Bertka, and B.O. Mysen, Eds., Mantle Petrology: Field Observations and High Pressure Experimentation. The Geochemical Society, Special Publication, 6, 125-153.

Hayman, P.C., Kopylova, M.G., and Kaminsky, F.V. (2005) Lower mantle diamonds from Rio Soriso (Juina area, Mato Grosso, Brazil) Contributions to Mineralogy and Petrology, 149, 430-445.

Hutchison, M.T. (1997) Composition of the deep transition zone and lower mantle shown by diamonds and their inclusions, 646 p. Ph.D. thesis, University of Edinburgh.

Irifune, T., Fujino, K., and Ohtani, E. (1991). A new high-pressure form of $MgAl_2O_4$. Nature, 349(6308), 409–411.

Irifune, T., Naka, H., Sanehira, T., Inoue, T., and Funakoshi, K. (2002). In situ X-ray observations of phase transitions in $MgAl_2O_4$ spinel to 40 GPa using multi anvil apparatus with sintered diamond anvils. Physics and Chemistry of Minerals, 29(10), 645–654.

578 Ishii, T., Kojitani, H., Tsukamoto, S., Fujino, K., Mori, D., Inaguma, Y., Tsujino, N.,
579 Yoshino, T., Yamazaki, D., Higo, Y., Funakoshi, K., and Akaogi, M. (2014) High-pressure
580 phase transitions in $FeCr_2O_4$ and structure analysis of new post-spinel $FeCr_2O_4$ and $Fe_2Cr_2O_5$
581 phases with meteoritical and petrological implications. American Mineralogist, 99, 1788-
582 1797.
583
584 Ishii, T., Kojitani, H., Fujino, K., Yusa, H., Mori, D., Inaguma, Y., Matsushita, Y., Yamaura,
585 K., and Akaogi, M. (2015) High-pressure high-temperature transitions in $MgCr_2O_4$ and
586 crystal structures of new $Mg_2Cr_2O_5$ and post-spinel $MgCr_2O_4$ phases with implications for
587 ultrahigh-pressure chromitites in ophiolites. American Mineralogist, 100, 59-65.
588
589 Ishii, T., Uenver-Thiele, L., Woodland, A., Alig, E., and Boffa Ballaran, T. (2018) Synthesis
590 and crystal structure of Mg-bearing Fe_9O_{11}: New insights in the complexity of Fe-Mg oxides
591 at conditions of the deep upper mantle. American Mineralogist, 103, 1873-1876.
592
593 Ishii, T., Miyajima, N., Sinmyo, R., Kojitani, H., Mori, D., Inaguma, Y., and Akaogi, M.
594 (2020) Discovery of new-structured post-spinel $MgFe_2O_4$: Crystal structure and high-pressure
595 phase relations. Geophysical research letters, 47, e2020GL087490. doi:
596 10.1029/2020GL087490
597
598 Jacob, D.E., Wirth, R., Enzmann, F., Kronz, A., and Schreiber, A. (2011) Nano-inclusion
599 suite and high resolution micro-computed-tomography of polycrystalline diamond (framesite)
600 from Orapa, Botswana. Earth and Planetary Science Letters, 308, 307-316.
601

602 Jacob, D.E., Piazolo, S., Schreiber, A., and Trimby, P. (2016) Redox-freezing and nucleation
603 of diamond via magnetite formation in the Earth's mantle. Nature communications, 7: 11891.
604 doi: 10.1038/ncomms11891
605
606 Katayama, I., and Iseda, A. (2002) Thermodynamic study of spinel-type solid solutions of the
607 Fe_3O_4-$MgFe_2O_4$ coexisting with Fe_2O_3 by emf method. Scandinavian Journal of Metallurgy,
608 31, 374-378.
609
610 Kawai, N., and Endo, S. (1970) The generation of ultrahigh hydrostatic pressures by a split
611 sphere apparatus. Rev. Sci. Instruments, 41, 1178-1181.
612
613 Keil, K. (2012) Angrites, a small but diverse suite of ancient, silica-undersaturated volcanic-
614 plutonic mafic meteorites, and the history of their parent asteroid. Chemie der Erde, 72, 191-
615 218.
616
617 Keppler, H., and Frost, D.J. (2005) Introduction to minerals under extreme conditions. In R.
618 Miletich, Ed., Mineral Behaviour at Extreme Conditions. EMU Notes in Mineralogy, 7, 1-30.
619
620 Krot, A.N. (2019) Refractory inclusions in carbonaceous chondrites: records of early solar
621 system processes. Meteoritics & Planetary Science, 1-45, doi: 10.1111/maps.13350.
622
623 Kaminsky, F., Wirth, R., Matsyuk, S., Schreiber, A., and Thomas, R. (2009) Nyerereite and
624 nahcolite inclusions in diamond: evidence for lower-mantle carbonatitic magmas.
625 Mineralogical Magazine, 73, 5, 797-816. doi: 10.1180/minmag.2009.073.5.797.
626

627 Kaminsky, F.V., Wirth, R., and Schreiber, A. (2015) A microinclusion of lower-mantle rock
628 and other minerals and nitrogen lower-mantle inclusions in a diamond. Canadian
629 Mineralogist, 53, 1, 83-104. doi: 0.3749/canmin.1400070.
630
631 Katayama, I., and Iseda, A. Thermodynamic study of spinel-type solid solutions of the
632 Fe3O4-$MgFe_2O_4$ coexisting with Fe_2O_3 by emf method. Sandinavian Journal of Mettalurgy,
633 31, 374-378.
634
635 Larson, A.C., and Von Dreele, R.B. (1994) GSAS General Structure Analysis System. Los
636 Alamo National Laboratory, New Mexico, USA.
637
638 Lavina, B., Dera, P., Kim, E., Meng, Y., Downs, R.T., Weck, P.F., Sutton, S.R., and Zhao, Y.
639 (2011) Discovery of the recoverable high-pressure iron oxide Fe_4O_5. Proceedings of the
640 National Academy of Science, 108, 17281-17285.
641
642 Lavina, B., and Meng, Y. (2015) Unraveling the complexity of iron oxides at high pressure
643 and temperature: Synthesis of Fe_5O_6. Science Advances, 1, No.5, e1400260.
644
645 Levy, D., Diella, V., Dapiaggi, M., Sani, A., Gemmi, M., and Pavese, A. (2004) Equation of
646 state, structural behavior and phase diagram of synthetic $MgFe_2O_4$, as a function of pressure
647 and temperature. Physics and Chemistry of Minerals, 31, 122-129.
648 Lorenzon, S., Wenz, M., Nimis, P., Jacobsen, S.D., Pasqualetto, L., Pamato, M., Novella, D.,
649 Zhang, D., Anzolini, C., Regier, M., Stachel, T., Pearson, D. G., Harris, J.W., Nestola, F.
650 (2023) Dual origin of ferropericlase inclusions within super-deep diamonds. Earth and
651 Planetary Science Letters, 608, 118081.
652

Ma, C., and Tschauner, O. (2017) Chenmingite, IMA 2017-036. CNMNC Newsletter No. 38, August 2017, page 1037; Mineralogical Magazine, 81, 1033-1038.

Ma, C., Tschauner, O., Beckett, J.R., Liu, Y., Greenberg, E., and Prakapenka, V.B. (2019) Chenmingite, $FeCr_2O_4$ in the $CaFe_2O_4$-type structure, a shock-induced, high-pressure mineral in the Tissint martian meteorite. American Mineralogist, 104, 1521-1525. doi: 10.2138/am-2019-6999.

Makovicky, E. (1977) Chemistry and crystallography of the lillianite homologous series. Part III: Crystal chemistry of lillianite homologues. Related phases. Neues Jahrbuch für Mineralogie Abhandlungen, 131, 187–207.

McCammon, C., Peyronneau, J., and Poirier, J.-P. (1998) Low ferric iron content of (Mg,Fe)O at high pressures and tempertaures. Geophysical Research Letters, 25, 1589-1592.

Myhill, B., Ojwang, D.O., Ziberna, L., Frost, D., Boffa Ballaran, T., and Miyajima, N. (2016). On the P-T-fO_2 stability of Fe_4O_5 and Fe_5O_6-rich phases: a thermodynamic and experimental study. Contributions to Mineralogy and Petrology, 171, 1-11.

Newhouse, W.H., and Glass, J.P. (1936) Some physical properties of iron oxides. Economic Geology, 31, 699-711.

Newnham, R.E., and de Hann, Y.M. (1962) Refinement of the alpha Al_2O_3, Ti_2O_3, V_2O_3 and Cr_2O_3 structures. Zeitschrift für Kristallographie 117, 235-237.

678 Palot, M., Jacobsen, S.D., Townsend, J.P., Nestola, F., Marquardt, K., Miyajima, N., Harris,
679 J.W., Stachel, T., McCammon, C.A., and Pearson, D.G. (2016) Evidence for H_2O-bearing
680 fluids in the lower mantle from diamond inclusion. Lithos, 265, 237-243.
681
682 Passchier C.W., and Trouw, R.A.J. (2005) Mircotectonics. 366 p. Springer, Heidelberg.
683
684 Tobi, B.H. (2001) EXPGUI, a graphical user interface for GSAS. Journal of Applied
685 Crystallography, 34, 210-213.
686
687 Turnock, A.C., and Eugster, H.P. (1962). Fe-Al oxides: phase relationships below 1000 °C.
688 Journal of Petrology, 3, 533-565.
689
690 Schollenbruch, K., Woodland, A.B., and Frost, D.J. (2011) The stability of hercynite at high
691 pressures and temperatures. Physics and Chemistry of Minerals, 37, 137–143.
692
693 Shannon, R.D. (1976) Revised effective ionic radii and systematic studies of interatomic
694 distances in halides and chalcogenides. Acta Crystallographica, A32, 751.
695
696 Sharygin, V.V., Britvin, S.N., Kaminsky, F.V., Wirth, R., Nigmatulina, E.N., Yakovlev, G.A.,
697 Novoselov, K.A., and Murashko, M. (2021) Ellinaite, $CaCr_2O_4$, a new natural post-spinel
698 oxide from Hatrurim Basin, Israel, and Juína kimberlite field, Brazil. European Journal of
699 Mineralogy, 33, 727-742. doi: 10.5194/ejm-33-727-2021.
700
701 Shirey, S., Smit, K., Pearson, D., Walter, M., Aulbach, S., Brenker, F., Bureau, H., Burnham,
702 A., Cartigny, P., Chacko, T., Frost, D.J., Hauri, E., Jacob, D.E., Jacobsen, S.D., Kohn, S.,
703 Luth, R.W., Mikhail, S., Navon, O., Nestola, F., Nimis, P., Palot, M., Smith, E.M., Stachel,

T., Stagno, V., Steele, A., Stern, R.A., Thomassot, E., Thomson, A.R., and Weiss, Y. (2019). Diamonds and the Mantle Geodynamics of Carbon: Deep Mantle Carbon Evolution from the Diamond Record. In B. Orcutt, I. Daniel, & R. Dasgupta (Eds.), Deep Carbon: Past to Present (pp. 89-128). Cambridge: Cambridge University Press.

Sinmyo, R., Bykova, E., Ovsyannikov, S.V., McCammon, C., Kupenko, I., Ismailova, L., and Dubrovinsky (2016) Discovery of Fe_7O_9: a new iron oxide with a complex monoclinic structure. Nature Scientific Reports, 6, 32852.

Smith, E.M., Shirey, S.B., Richardson, S.H., Nestola, F., Bullock, E.S., Wang, J., and Wang, W. (2018) Blue boron-bearing diamonds from Earth's lower mantle. Nature, 560, 84-87.

Stachel, T., Harris, J.W., and Brey, G.P. (1998) Rare and unusual mineral inclusions in diamonds from Mwadui, Tanzania. Contributions to Mineralogy and Petrology, 132, 34-47.

Uenver-Thiele, L., Woodland, A.B., Boffa Ballaran, T., Miyajima, N., and Frost, D.J. (2017a) Phase relations of $MgFe_2O_4$ at conditions of the deep upper mantle and transition zone. American Mineralogist, 102, 632-642.

Uenver-Thiele, L., Woodland, A.B., Boffa Ballaran, T., Miyajima, N., and Frost, D.J. (2017b) Phase relations of Fe-Mg spinels including new high-pressure post-spinel phases and implications for natural samples. American Mineralogist, 102, 2054-2064.

Uenver-Thiele, L. Woodland, A.B, Miyajima, N., Boffa Ballaran, T., Frost, D.J. (2018) Behaviour of Fe_4O_5-$Mg_2Fe_2O_5$ solid solutions and their relation to coexisting Mg-Fe silicates and oxide phases. Contributions to Mineralogy and Petrology 173:20.

Walker, D., Carpenter, M.A., and Hitch, C.M. (1990) Some simplifications to multianvil devices for high-pressure experiments. American Mineralogist, 75, 1020-1028.

Wirth, R., Dobrzhinetskaya, L., Harte, B., Schreiber, A., and Green, H.W. (2014) High-Fe (Mg,Fe)O inclusion in diamond apparently from the lowermost mantle. Earth and Planetary Science Letters 404, 365-375.

Woodland, A.B., Frost, D.J., Trots, D.M., Klimm, K., and Mezouar, M. (2012) In situ observation of the breakdown of magnetite (Fe_3O_4) to Fe_4O_5 and hematite at high pressures and temperatures. American Mineralogist, 97, 1808-1811.

Woodland,A.B., Uenver-Thiele, L., and Boffa Ballaran, T. (2015) Synthesis of Fe_5O_6 and the high-pressure stability of Fe^{2+}-Fe^{3+}-oxides related to Fe_4O_5. Goldschmidt Abstracts, 3446.

Woodland, A.B., Uenver-Thiele, L., Boffa Ballaran, T., Miyajima, N., Roßbach, K., and Ishii, T. (2023). Stability of Fe_5O_6 and its relation to other Fe-Mg-oxides at high pressures and temperatures. American Mineralogist, 108, 140-149. doi: 10.2138/am-2022-8370.

Yong, W., Botis, S., Shieh, S.R., Shi, W., and Withers, A.C. (2012) Pressure-induced phase transition study of magnesiochromite ($MgCr_2O_4$) by Raman spectroscopy and X-ray diffraction. Physics of the Earth and Planetary Interiors, 196-197, 75-82.

Zhang, D. 2017 Making a fine-scale ruler for oxide inclusions. American Mineralogist, 102, 1969-1970.

FIGURE CAPTION

Figure 1. Backscatter electron images of the experimental run products showing a) the assemblage of well-crystallized cor_{ss} + hem_{ss} + $Fe_2(Fe,Al)_2O_5$, b) coexistence of large crystals of $Fe_3(Fe,Al)_4O_9$ with interstitial cor_{ss} + hem_{ss}, c) crystals of cor_{ss} and a striated high-pressure post-spinel phase, presumably hp-O_4, that have transformed during quenching into defect magnetite (dmt; see text for details), d) run products of Z1953o with an UQ-phase coexisting with the same dmt as in (c). The dmt has slightly variable contrast due to effects of composition as well as orientation, and is full of striations, comparable to those observed in (c). Note that the UQ-phase differs from dmt by its texture (see text below for details). Abbreviations: hematite-corundum solid solutions are referred to as cor_{ss} or hem_{ss}; wü= wüstite; UQ-phase= unquenchable phase; [hp-O_4] = spinel phase with a high magnetite component formed presumably by retrograde reaction from a high-*P* polymorph during quench.

Figure 2. Phase stabilities for the bulk composition $Fe^{2+}(Fe^{3+}_{0.8}Al_{0.2})_2O_4$. The boundaries of the assemblage stability fields are delineated by solid lines. The dashed black line indicates the breakdown reaction for magnetite which was observed in situ by Schollenbruch et al. (2011) and later identified by Woodland et al. (2012). Also shown is the position of the breakdown reaction for hercynite (dotted line) from Schollenbruch et al. (2010). The errors in P and T are approximately equal to the size of the symbol. Note: Experiment Z1953o at 20 GPa and 1300 °C contains an additional UQ-phase (see also Fig. 1d).

Figure 3. (a) Bright-field (BF) TEM image of sample Z1953o illustrating the assemblage of dmt + UQ-phase. (b) BF-TEM image of the dmt phase [right grain in the BF-TEM in (a)] with numerous lamellae normal to the projection of the {100} plane. The inset shows the

781 corresponding precession selected area electron diffraction (SAED) pattern (circle), indicating
782 a superimposition of the <011> and the <121> zone axes of magnetite. The two zone axes
783 have a common direction along <011> (the diagonal direction from the lower left to upper
784 right in the electron diffraction pattern). Note that the indexing is with the <011> zone axis of
785 magnetite. (c) Dark-field TEM image (with $\boldsymbol{g}$-vectors of 400 from the matrix and twins) of the
786 lamella-bearing dmt phase [the center one in image (a)] displaying {113} twin lamellae. The
787 inset shows a SAED pattern indicating the twin relation.
788
789 Figure 4. (a) High-angle annular dark-field (HAADF) STEM image illustrating the dmt phase
790 (left-hand side) next to the fine-grained unquenchable domains (right-hand side) and (b) EDS
791 chemical map of the UQ-domain indicating Al-dominant and Fe-dominant dissociation
792 products. (c) BF-TEM images of the Al-dominant phase indexed with a corundum structure
793 (Crn) shown in the lower right inset. (d) BF-TEM images of the Fe-dominant phase. A
794 selected area electron diffraction (SAED) pattern was taken in the area indicated by the white
795 circle that is consistent with magnetite. Noteably, this magnetite does not have the features of
796 a defect magnetite structure.
797
798 Figure 5. Lattice parameters of $Fe_2Fe_2O_5$-$Fe_2Al_2O_5$ solid solutions as a function of Al content
799 (cpfu). These solid solutions adopt the same $CaFe_3O_5$-type structure (Cmcm space group) as
800 $Mg_2Fe_2O_5$ reported by Boffa Ballaran et al. (2015). Variation in a) molar volume, b) *a*-
801 parameter, c) *b*-parameter and d) *c*-parameter with the amount of Al in the crystal structure.
802 For comparison, lattice parameters of the endmember Fe_4O_5 from the study by Wooland et al.
803 (2022) are also shown. Error bars are within the size of the symbols.
804

Figure 6. Plot of the $Fe^{3+}/(Fe^{3+}+Al)$ of Al-bearing hematite and Fe-bearing corundum as a function of synthesis temperature. Experimental results obtained in the studies by Feenstra et al. (2005) at 1-40 kbar, Turnock & Eugster (1962) at 2-4 kbar and Atlas & Sumida (1958) at 1 bar are also shown for comparison.

Figure 7. Lattice parameter a (a), lattice parameter c (b) as well as volume (c) plotted versus chemical composition of corundum-hematite solid solutions. Insets show enlargements. Dashed lines show linear mixing between synthetic Al_2O_3 and Fe_2O_3 (Finger and Hazen, 1980; Newnham and de Hann, 1962).

This is the peer-reviewed, final accepted version for American Mineralogist, published by the Mineralogical Society of America.
The published version is subject to change. Cite as Authors (Year) Title. American Mineralogist, in press.
DOI: https://doi.org/10.2138/am-2023-8948. http://www.minsocam.org/

Table 1. Experimental conditions and run products

Experiment	Pressure [GPa]	Temperature [C°]	Duration [h]	Phase assemblage
$Fe(Al_{0.2}Fe_{0.8})_2O_4$				
M798*	6	1200	3	O_4
M808	8	1300	2.5	O_4
M830	9	1400	1	O_4
M840	9	1100	3	O_4
M804*	11	1300	2	O_5 + cor_{ss} + FeO
M789	12	1300	1.5	O_5 + hem_{ss} + cor_{ss}
M788	14	1200	2.5	O_5 + hem_{ss} + cor_{ss}
M790	14	1400	1.5	O_5 + hem_{ss} + cor_{ss}
Z2039u*	15	1200	3	O_5 + cor_{ss} + (sid)
Z2031o*	16	1200	3	O_5 + cor_{ss} + (hem_{ss}) + (sid)
Z2030o*	16	1500	1	O_5 + cor_{ss} + (sid)
M823*	18	1200	2.5	[hp-O_4] + cor_{ss}
M825*	18	1300	2	O_5 + cor_{ss}
M841	18	1300	2	O_9 + [hp-O_4] + cor_{ss}
Z2040u*	18	1400	1	O_9 + hem_{ss} + cor_{ss}
Z1953o	20	1300	1	[hp-O_4] + cor_{ss} + UQ
S7317	20	1550	1.5	O_5 + cor_{ss}
H5668	20	1400	1.5	O_9 + cor_{ss}
S7316	22	1300	1.5	[hp-O_4] + cor_{ss}
H5745	22	1450	1 min	O_9 + cor_{ss}
$Fe(Al_{0.4}Fe_{0.6})_2O_4$				
M815*	14	1400	1.5	O_5 + cor_{ss} + (O_6)
M822	18	~1250	2	O_9 + cor_{ss} + (sid)
$Fe(Al_{0.6}Fe_{0.4})_2O_4$				
M842	10	1200		O_4 + (O_5) + (hem_{ss}) + (cor_{ss})
M826	13	1200	3	O_5 + cor_{ss}
M843	14	1400	1.5	O_5 + cor_{ss}
$Fe_3Fe_3AlO_9$				
M844	18	1400	1.5	O_5 + cor_{ss} + (sid)
M784	18	1500	1	O_5 + cor_{ss} + (sid)

Notes: * Experiment performed with a Pt-capsule; O_4: cubic $Fe(Al,Fe)_2O_4$; O_5: orthorhombic $Fe_2(Al,Fe)_2O_5$ phase; O_9: monoclinic $Fe_3(Al,Fe)_4O_9$ phase; wü: wüstite; UQ=unquenchable phase that dissociated into Fe^{3+}-bearing corundum + nearly pure magnetite; sid= siderite; hematite-corundum solid solutions are referred to as cor_{ss} or hem_{ss}; phases in parentheses = only present in traces; phase in brackets = assumed high-pressure polymorph that reacted back to defect-magnetite during quenching

This is the peer-reviewed, final accepted version for American Mineralogist, published by the Mineralogical Society of America.
The published version is subject to change. Cite as Authors (Year) Title. American Mineralogist, in press.
DOI: https://doi.org/10.2138/am-2023-8948. http://www.minsocam.org/

Table 2. Unit cell parameters of $Fe(Fe,Al)_2O_4$, $Fe_2(Fe,Al)_2O_5$ and $Fe_3(Fe,Al)_4O_9$

Experiment	nAl	lattice parameters				
	[c.p.f.u.]	*a* [Å]	*b* [Å]	*c* [Å]	V [Å³]	β [°]
			Fe(Fe,Al)$_2$O$_4$			
M798	0.38(1)	8.3464(1)			581.423(14)	
M830	0.39(3)	8.3387(1)			579.822(10)	
M840	0.41(1)	8.3379(1)			579.66(2)	
M808	0.44(2)	8.3421(1)			580.54(2)	
M842	0.85(1)	8.2901(1)			569.75(3)	
			defect-Fe(Fe,Al)$_2$O$_4$ [1]			
Z1953o	0.10(1)	8.3783(1)			588.11(2)	
S7316	0.11(1)	-			-	
M823	0.11(1)	8.3830(1)			589.11(2)	
M841	0.14(1)	8.3697(4)			586.31(9)	
			Fe$_2$(Fe,Al)$_2$O$_5$			
M788	0.07(1)	2.8928(1)	9.7820(3)	12.5678(4)	355.632(12)	
M789	0.09(1)	2.8945(1)	9.7750(2)	12.5671(2)	355.572(8)	
M790	0.11(1)	2.8938(1)	9.7676(2)	12.5633(2)	355.109(8)	
M825	0.12(1)	2.8946(1)	9.7632(2)	12.5593(2)	354.934(8)	
Z2039u	0.12(1)	2.8933(1)	9.7634(3)	12.5557(3)	354.683(10)	
M843	0.12(1)	2.8937(1)	9.7725(2)	12.5640(2)	355.289(7)	
M826	0.13(1)	2.8939(1)	9.7654(2)	12.5580(2)	354.900(7)	
M844	0.14(1)	2.8942(1)	9.7582(3)	12.5582(3)	354.670(11)	
M784	0.17(1)	2.8941(1)	9.7545(2)	12.5491(2)	354.270(6)	
M804	0.17(1)	2.8933(1)	9.7588(5)	12.5558(5)	354.51(2)	
M815	0.20(1)	2.8929(1)	9.7495(3)	12.5484(4)	353.923(14)	
Z2030o	0.23(1)	2.8934(1)	9.7449(2)	12.5435(2)	353.667(7)	
Z2031o	0.23(1)	2.8937(1)	9.7699(3)	12.5647(3)	355.223(10)	
S7317	0.30(1)	2.8924(1)	9.7316(5)	12.5334(5)	352.780(18)	
			Fe$_3$(Fe,Al)$_2$O$_6$			
M815	-	2.8936(3)	9.8707(12)	15.3316(14)	437.89(5)	
			Fe$_3$(Fe,Al)$_4$O$_9$			
Fe_7O_9 [2]	0.00	9.696(2)	2.8947(6)	11.428(3)	314.10(12)	101.69(2)
M841	0.22(1)	9.6784(3)	2.8991(1)	11.4112(4)	313.545(14)	101.685(3)
Z2040u	0.23(1)	9.6717(4)	2.8961(1)	11.4222(4)	313.248(14)	101.741(3)
H5668	0.28(1)	9.6732(2)	2.8960(1)	11.4127(3)	313.042(9)	101.726(2)
M822	0.33(1)	9.6683(3)	2.8930(7)	11.3925(3)	312.00(1)	101.729(2)
H5745	0.42(2)	9.6604(9)	2.8919(2)	11.3965(9)	311.74(3)	101.725(6)

[1] defect-magnetite phase with relict features of an presumably hp-polymorph and an Al-poor composition
[2] endmember data from Sinmyo et al. (2016)

This is the peer-reviewed, final accepted version for American Mineralogist, published by the Mineralogical Society of America.
The published version is subject to change. Cite as Authors (Year) Title. American Mineralogist, in press.
DOI: https://doi.org/10.2138/am-2023-8948. http://www.minsocam.org/

Table 3. Unit cell parameters of corundum-hematite solid solutions

Experiment	corundum				hematite			
	$(Fe^{3+}/Fe^{3+}+Al)$	*a* [Å]	*c* [Å]	V_{mol} [cm^3/mol]	$(Fe^{3+}/Fe^{3+}+Al)$	*a* [Å]	*c* [Å]	V_{mol} [cm^3/mol]
M842	0.040	-	-	-	0.985	-	-	-
M804*	0.045	4.7694(3)	13.014(1)	256.37(3)				
M815	0.045	4.7711(3)	13.018(2)	256.64(4)				
M826	0.045	4.7672(1)	13.0084(5)	256.030(9)				
Z2030o	0.045	4.7733(7)	13.012(3)	256.75(7)				
M825	0.055	4.7698(1)	13.0141(5)	256.42(1)				
Z2031o	0.065	4.7676(5)	13.018(2)	256.25(4)	0.970	-	-	-
M784	-	4.7749(2)	13.0310(8)	257.30(2)				
M823	0.065	4.7768(2)	13.0333(8)	257.55(2)				
M841	0.070	4.7800(3)	13.0428(11)	258.08(2)				
S7316	0.075	-	-	-				
M788	-	4.7820(3)	13.0407(2)	258.25(3)	0.850	4.9985(1)	13.6336(5)	295.000(11)
Z2039u	0.080	4.7698(2)	13.0148(10)	256.43(2)				
Z1953o	-	4.7845(4)	13.0290(10)	258.29(3)				
M843	0.090	4.7854(1)	13.0501(4)	258.810(8)				
M844	0.090	4.7797(3)	13.0439(12)	258.08(3)				
M822	0.095	4.7896(1)	13.0656(5)	259.570(9)				
M789	0.105	4.7900(2)	13.0564(10)	259.43(2)	0.815	4.9892(1)	13.6056(7)	293.30(2)
H5668	0.100	4.7897(2)	13.0612(10)	259.50(2)				
S7317	0.110	4.7858(8)	13.057(4)	258.99(7)				
H5745	0.115	4.7901(4)	13.0725(2)	259.76(3)				
Z2040u	0.120	4.7976(4)	13.0845(12)	260.82(3)	0.820	4.9714(3)	13.604(3)	291.18(6)
M790	0.145	4.7996(2)	13.0825(8)	260.99(2)	0.765	4.9741(2)	13.5698(9)	290.76(2)

* wüstite has been detected with lattice parameters of a = 4.2718(2) Å and V_{mol} = 77.953(12) cm^3/mol

Figure 1

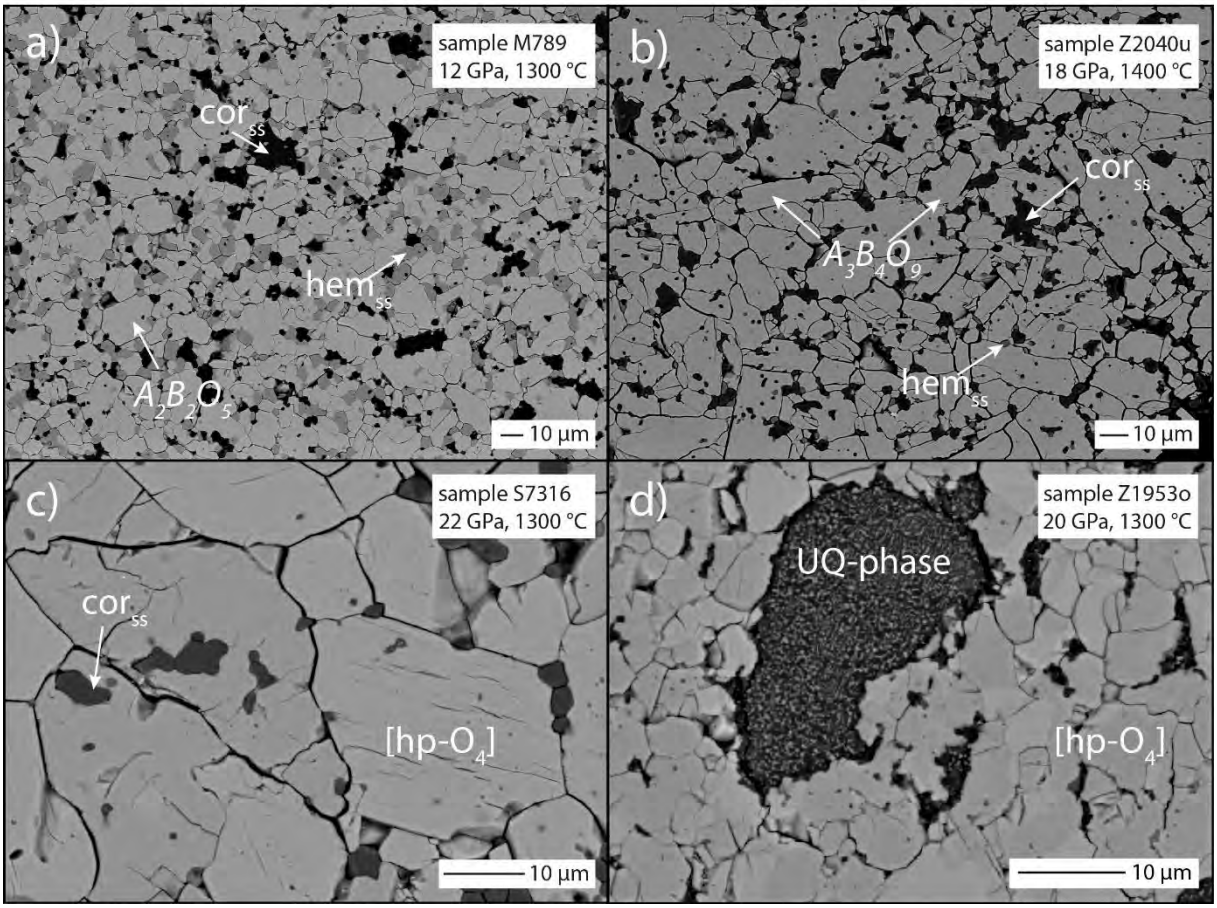

This is the peer-reviewed, final accepted version for American Mineralogist, published by the Mineralogical Society of America.
The published version is subject to change. Cite as Authors (Year) Title. American Mineralogist, in press.
DOI: https://doi.org/10.2138/am-2023-8948. http://www.minsocam.org/

Figure 2

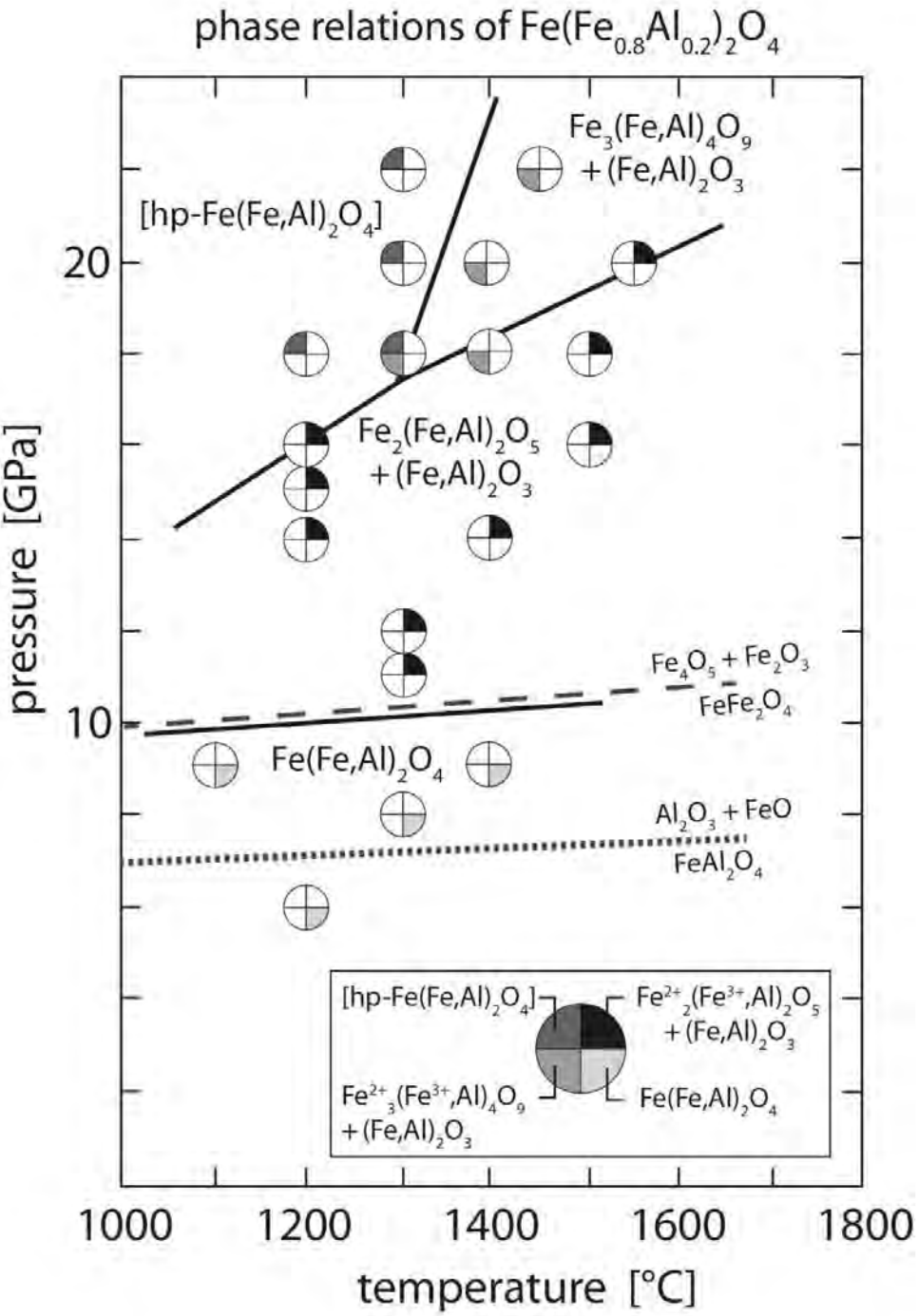

Figure 3

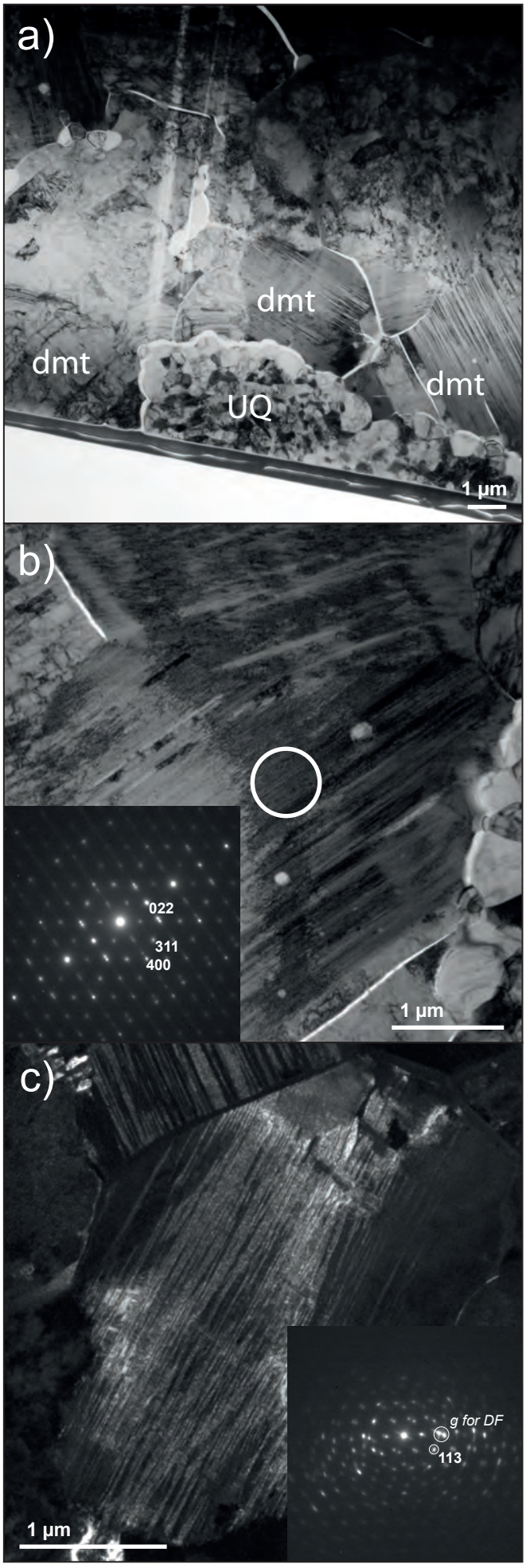

This is the peer-reviewed, final accepted version for American Mineralogist, published by the Mineralogical Society of America.
The published version is subject to change. Cite as Authors (Year) Title. American Mineralogist, in press.
DOI: https://doi.org/10.2138/am-2023-8948. http://www.minsocam.org/

Figure 4

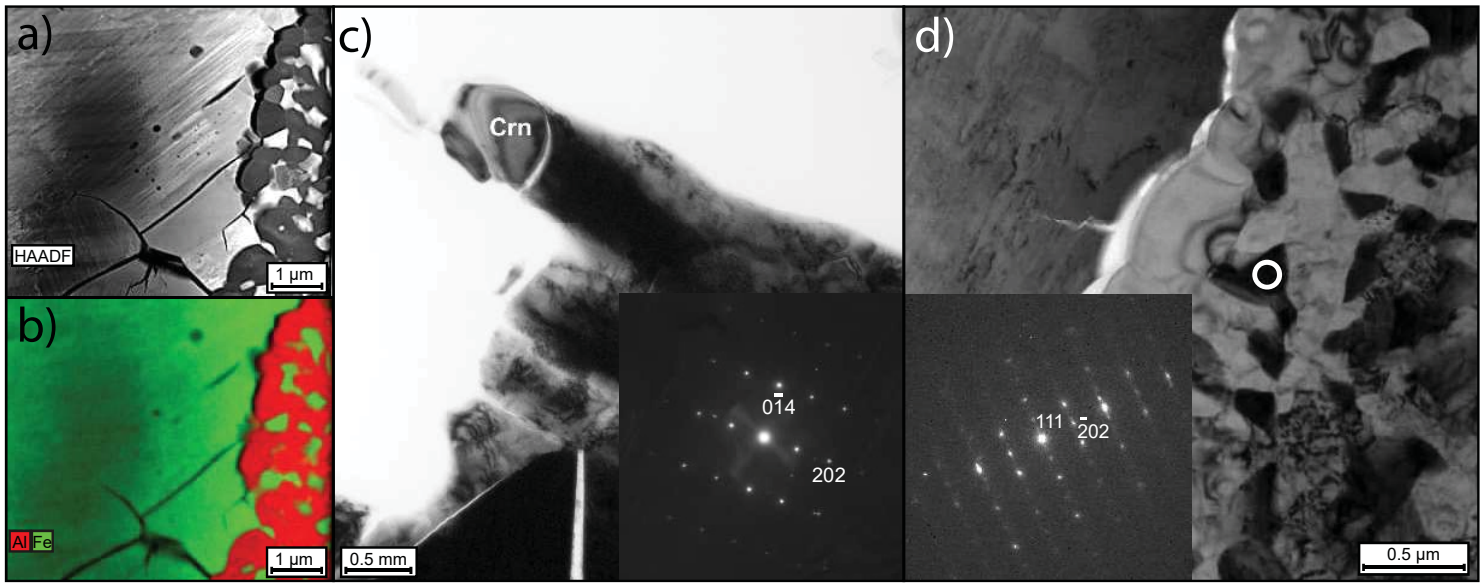

This is the peer-reviewed, final accepted version for American Mineralogist, published by the Mineralogical Society of America.
The published version is subject to change. Cite as Authors (Year) Title. American Mineralogist, in press.
DOI: https://doi.org/10.2138/am-2023-8948. http://www.minsocam.org/

Figure 5

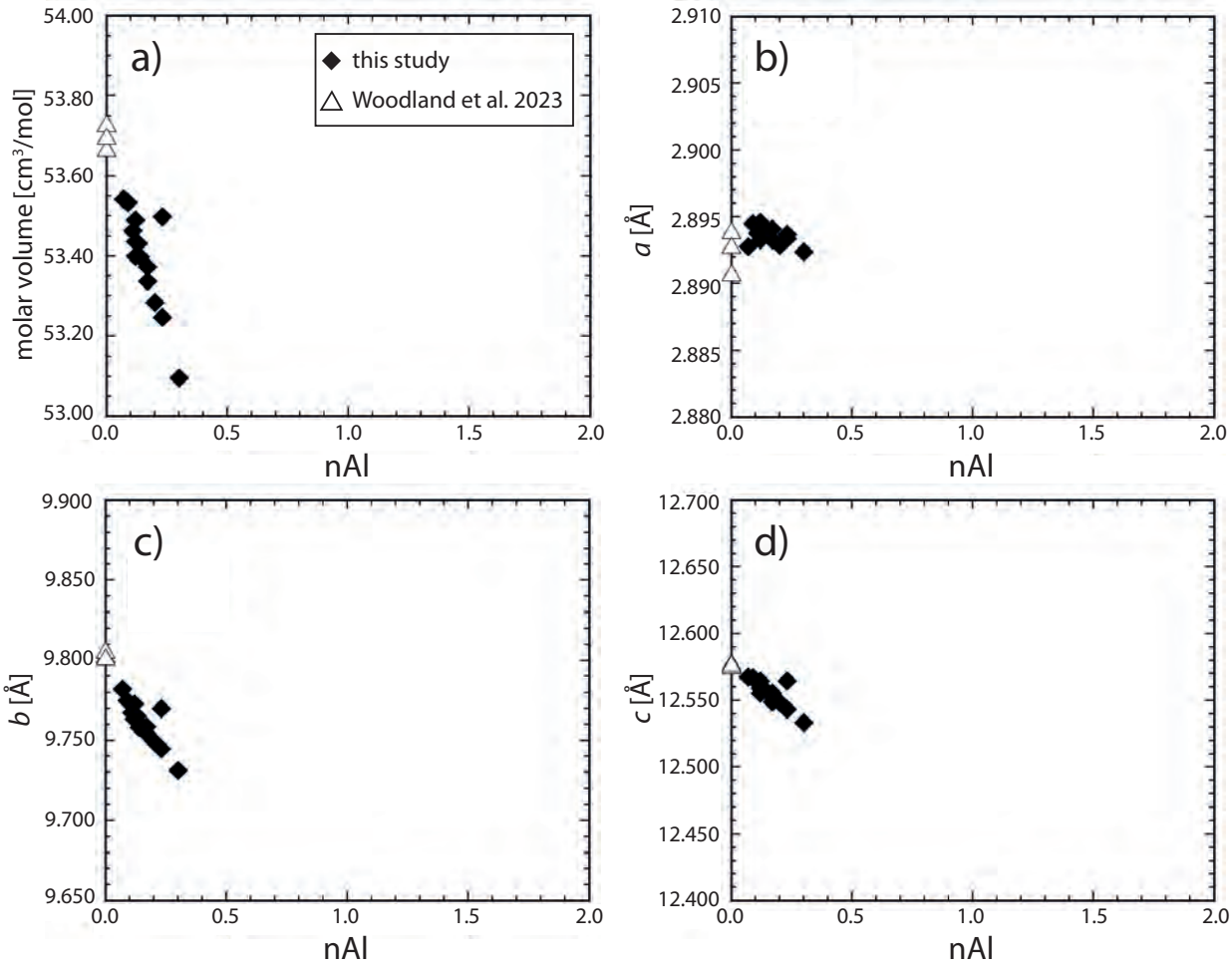

Figure 6

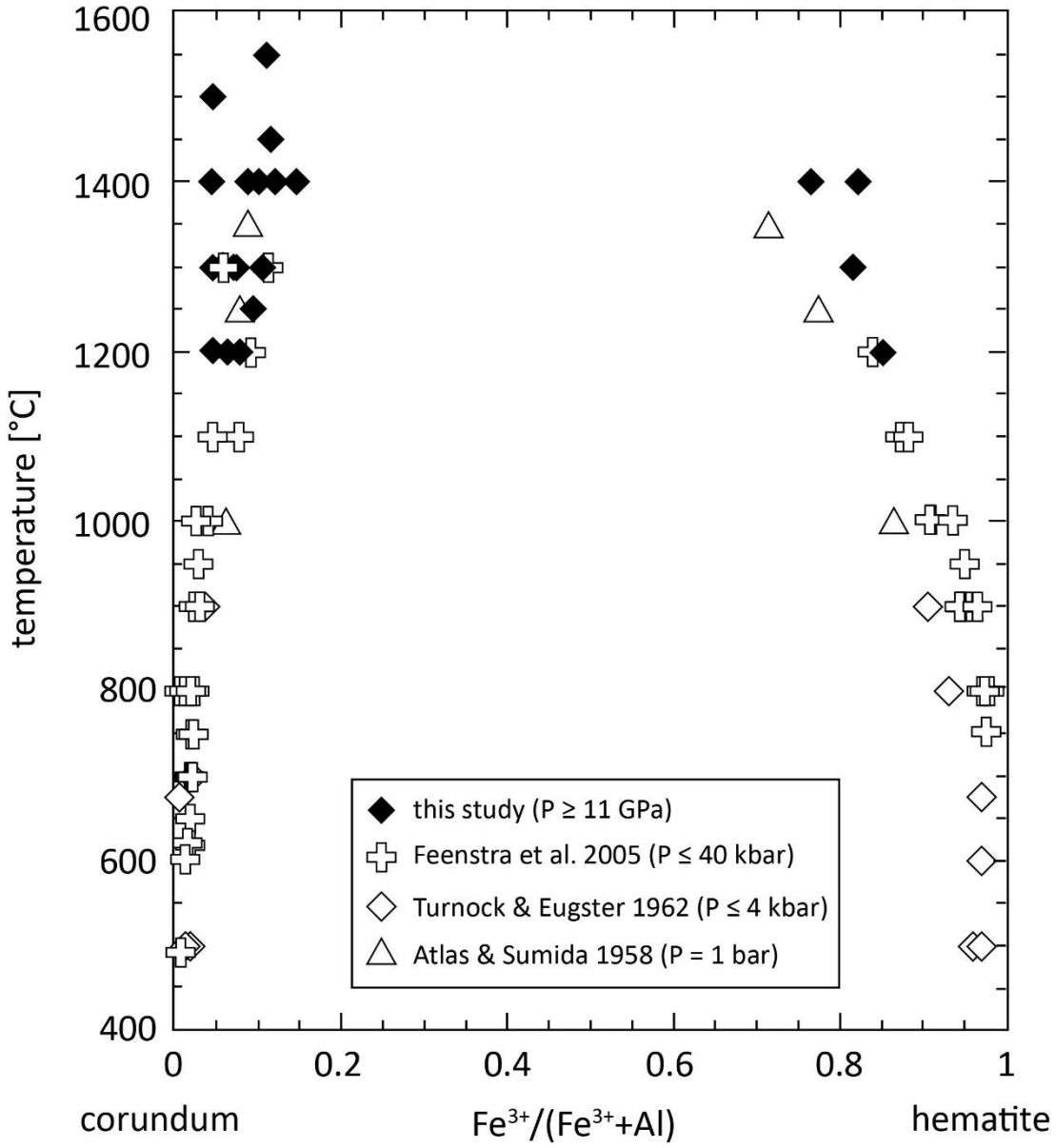

This is the peer-reviewed, final accepted version for American Mineralogist, published by the Mineralogical Society of America.
The published version is subject to change. Cite as Authors (Year) Title. American Mineralogist, in press.
DOI: https://doi.org/10.2138/am-2023-8948. http://www.minsocam.org/

Figure 7